Structural Engineering and Mechanics, Vol. 39, No. 3 (2011) 339-360
DOI: http://dx.doi.org/10.12989/sem.2011.39.3.339

New slave-node constraints and element for adaptive analysis of C^0 plates

K.Y. Sze*[1] and D. Wu[1,2a]

[1]*Departments of Mechanical Engineering, The University of Hong Kong, Pokfulam, Hong Kong, P.R. China*
[2]*Altair Engineering Software (Shanghai), Suite 1401-06, 248 Yangshupu Road, Shanghai 200082, China*

(Received June 18, 2010, Accepted April 8, 2011)

Abstract. In the *h*-type adaptive analysis, when an element is refined or subdivided, new nodes are added. Among them are the transition nodes which are the corner nodes of the new elements formed by subdivision and, simultaneously, the mid-side nodes of the adjacent non-subdivided elements. To secure displacement compatibility, the slave-node approach in which the DOFs of a transition node are constrained by those of the adjacent nodes had been used. Alternatively, transition elements which possess the transition nodes as active mid-side/-face nodes can be used. For C^0 plate analyses, the conventional slave-node constraints and the previously derived ANS transition elements are implemented. In both implementations, the four-node element is the ANS element. With reference to the predictions of the transition elements, the slave-node approach not only delivers erroneous results but also fails the patch test. In this paper, the patch test failure is resolved by developing a set of new constraints with which the slave-node approach surpasses the transition-element approach. The accuracy of the slave-node approach is further improved by developing a hybrid four-node element in which the assumed moment and shear force modes are in strict equilibrium.

Keywords: plate bending, transition element; constraints; adaptive analysis; slave node; hybrid

1. Introduction

Since 1960s, considerable efforts have been devoted to plate bending element formulation. Most of the earliest plate elements were developed based on Kirchhoff theory which requires the transverse deflection to be C^1 across the element boundaries. Later, Reissner-Mindlin plate elements received much attention. They are also known as C^0 elements as their transverse deflections need only to be C^0 and can be constructed by simple interpolation. However, shear locking is often encountered by the conventional C^0 elements. Among various techniques for overcoming the shear locking, the MITC (mixed interpolated tensorial covariant strain) or ANS (assumed natural strain) methods construct the transverse shear strain field by sampling the transverse shear strains along the element edges (Dvorkin and Bathe 1984, Bathe and Dvorkin 1985, Huang and Hinton 1986, Park and Stanley 1986, Donea and Lamain 1987, Sze and Zhu 1998). In doing so, the number of independent sampled strains which constitute the numerical constraints to enforce the Kirchhoff

*Corresponding author, Professor, E-mail: kysze@hku.hk
[a]E-mail: danny.wudan@gmail.com

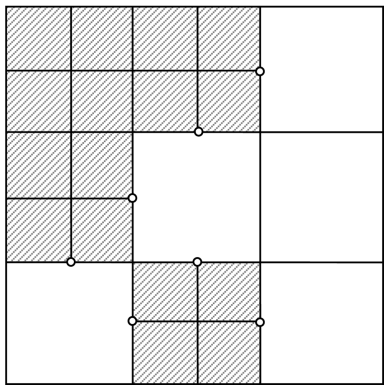

Fig. 1 A mesh with its transition nodes denoted by "*o*". The elements formed by sub-division are hatched

condition can be effectively reduced in the global level. On the other hand, the hybrid finite element method has also been employed to develop accurate C^0 plate elements. Though the equilibrium conditions couple the assumed moment and shear force modes, both coupled formulation (Lee and Pain 1978, Lee *et al.* 1985, Ayad *et al.* 1998) and uncoupled formulation (Saleeb and Chang 1987, Weissman and Taylor 1990, Sze 1994a) can be noted. In some lower order hybrid elements, the ANS method is also invoked to resolve shear locking. They can be termed as hybrid ANS elements (Ayad *et al.* 1998).

In finite element analysis, an optimized mesh is regarded as the mesh that yields the most accurate prediction for a fixed number of nodal DOFs. Optimized meshes can hardly be achieved before the advent of AFEM (adaptive finite element method). Among the three basic strategies of AFEM, i.e., *h*-type, *r*-type and *p*-type, *h*-type is the simplest one which will be pursued in this study. The *h*-type AFEM comprises three stages, namely (i) finite element analysis, (ii) stress recovery and error estimation, and (iii) mesh refinement. When an element is subdivided, new nodes are added to the mesh. Some of them are transition nodes which are the corner nodes of the new elements formed by subdivision and, simultaneously, the mid-side/mid-face nodes of the adjacent non-subdivided elements as shown in Fig. 1. To secure displacement compatibility, the slave-node and transition-element approaches have been employed.

The slave-node approach for plate adaptive analysis had been mentioned in a short communication by Somervaille (1973) in the early 1970's. Later, Devloo *et al.* (1987) presented a more detailed procedure for elasticity problems. They both constrained the displacements/rotations of the transition node to be the displacement/rotation average of the two corner nodes on the same element edge of the transition node. Since the transition nodes do not bring any improvement in accuracy and the employed constraints are highly standard, this approach has been remained intact in the last three decades to the best knowledge of the authors.

While there are many four-node C^0 plate elements, transition elements for adaptive plate analyses are rare. Same as all compatible transition elements, the displacements/rotations inside these elements are piecewise linear (Gupta 1978). Among them, a transition element family was developed by Choi and Park (1992) who employed an alternate set of formulae for the ANS scheme (Donea and Lamain 1987). They also presented an incompatible element family (Choi and Park 1997) which fails the constant moment patch test. However, the problem may be fixed by modifying the incompatible part of the strain-displacement matrix as in axisymmetric transition

element family of Choi and Lee (2004). Wan (2004) also developed a transition plate element family. The bending and transverse shear stiffness matrices of the elements are formulated by the hybrid finite element and the ANS methods, respectively. The assumed moment fields in the element families are the same as those of the transition element family for 2D elasticity problems (Wan 2004, Lo *et al.* 2006). However, the error estimation reveals that Wan's hybrid ANS transition element family is less accurate than the ANS transition family.

In an attempt to improve the transition element family of Wan who employed an uncoupled hybrid ANS formulation, Wan's uncoupled hybrid ANS family, a coupled hybrid ANS family, the ANS transition element family and the slave-node approach with the standard constraints (Somervaille 1973) were implemented. The popular four-node ANS element is employed in the slave-node approach. The two hybrid ANS element families and the slave-node approach yield less accurate results than the ANS element family. While the four-node ANS element passes the patch test, it is noted that the employed slave-node constraints leads to patch test failure. In this paper, the failure would be rectified by developing a new set of constraints with which the slave-node approach surpasses the ANS element family in accuracy. The accuracy is further improved by developing a four-node hybrid ANS element similar to but simpler than an existing element (Ayad *et al.* 1998) in which the assumed moment and shear force modes are in strict equilibrium. Numerical examples are presented to illustrate the improvement yielded by the new slave-node constraints and the new element.

2. Review of ANS elements

The four-node ANS C^0 plate bending element and the ANS transition element family (Bathe and Dvorkin 1985, Choi and Park 1992, Wan 2004) will be briefly reviewed in this section. It will also be seen that the ANS transverse shear strain is relevant to the new constraints in the slave-node approach.

2.1 The conventional four-node and transition elements

In C^0 plate bending elements, the displacement components u, v, w inside the element is governed by

$$u = z\theta_y(x,y), \quad v = -z\theta_x(x,y), \quad w = w_o(x,y) \tag{1}$$

in which θ_x, θ_y and w_o denotes the rotation about the x-axis, the rotation about the y-axis and the mid-plane transverse displacement along the z-axis. The rotations, the transverse displacement and coordinates of the four-node and various transition elements in Fig. 2 can be obtained by nodal interpolation as

$$\theta_x = \sum_{i=1}^{n} N_i\theta_{xi}, \quad \theta_y = \sum_{i=1}^{n} N_i\theta_{yi}, \quad w = \sum_{i=1}^{n} N_i w_{oi}, \quad x = \sum_{i=1}^{n} N_i x_i, \quad y = \sum_{i=1}^{n} N_i y_i \tag{2}$$

where n is the number of nodes in the element, N_i is the interpolation function and the subscript "i" denotes the affixed quantity at the i-th node. The set of piecewise linear interpolation functions for 2D transition elements which are strictly compatible with the adjacent linear elements are (Gupta 1978)

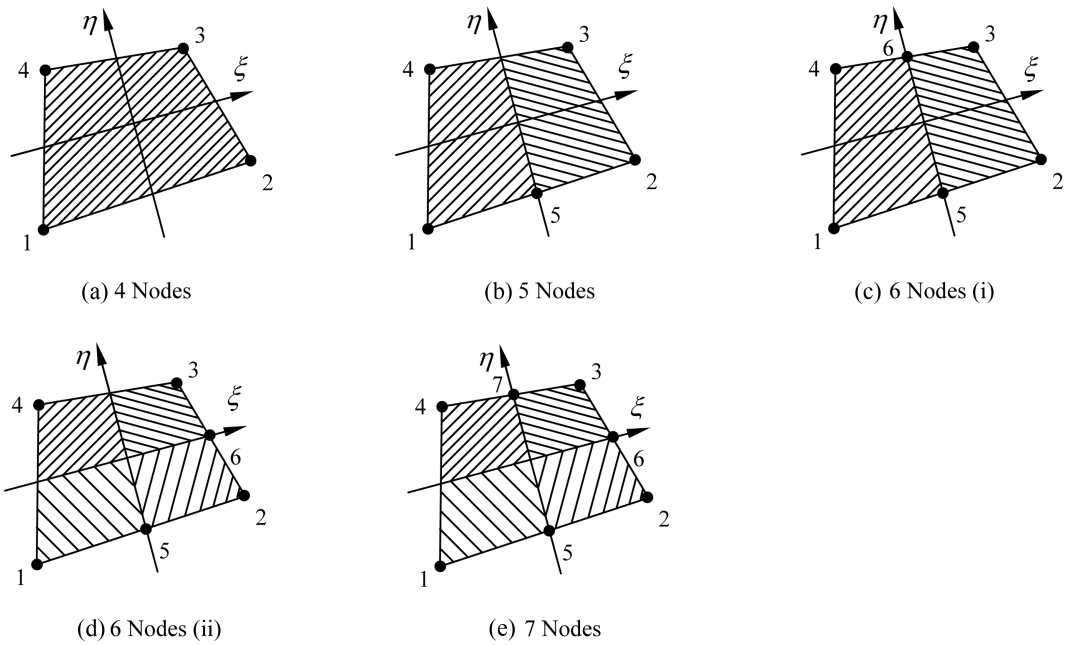

(a) 4 Nodes (b) 5 Nodes (c) 6 Nodes (i)

(d) 6 Nodes (ii) (e) 7 Nodes

Fig. 2 (a) Four-node element and (b)-(e) transition elements with different numbers of transition nodes. If exists, node 8 bisects the edge defined by nodes 1 and 4. Different integration zones are hatched differently

$$N_5 = \frac{\Delta_5}{2}(1-|\xi|)(1-\eta)\,,\quad N_6 = \frac{\Delta_6}{2}(1+\xi)(1-|\eta|)\,,\quad N_7 = \frac{\Delta_7}{2}(1-|\xi|)(1+\eta)\,,\quad N_8 = \frac{\Delta_8}{2}(1-\xi)(1-|\eta|)$$

$$N_1 = \frac{1}{4}(1-\xi)(1-\eta)-\frac{1}{2}(N_5+N_8)\,,\quad N_2 = \frac{1}{4}(1+\xi)(1-\eta)-\frac{1}{2}(N_5+N_6)$$

$$N_3 = \frac{1}{4}(1+\xi)(1+\eta)-\frac{1}{2}(N_6+N_7)\,,\quad N_4 = \frac{1}{4}(1-\xi)(1+\eta)-\frac{1}{2}(N_7+N_8) \tag{3}$$

where | | returns the absolute value of embraced term and

$$\Delta_i = \begin{cases} 1 \text{ if the } i\text{-th node exists} \\ 0 \text{ otherwise} \end{cases}$$

It can be checked that the functions degenerate into the common bilinear shape functions in the absence of any transition node. As the transition element is subparametric, the interpolated coordinates can be simplified to be

$$x = a_0 + a_1\xi + a_3\eta + a_2\xi\eta\,,\qquad y = b_0 + b_1\xi + b_3\eta + b_2\xi\eta \tag{4}$$

where a's and b's are linear combinations of the nodal coordinates. The Jacobi matrix and its determinant are

$$\mathbf{J} = \begin{bmatrix} \partial x/\partial\xi & \partial y/\partial\xi \\ \partial x/\partial\eta & \partial y/\partial\eta \end{bmatrix} = \begin{bmatrix} a_1 + a_2\eta & b_1 + b_2\eta \\ a_3 + a_2\xi & b_3 + b_2\xi \end{bmatrix},\quad J = \det(\mathbf{J}) = J_o + J_\xi\xi + J_\eta\eta \tag{5}$$

where $J_o = a_1 b_3 - a_3 b_1$, $J_\xi = a_1 b_2 - a_2 b_1$ and $J_\eta = a_2 b_3 - a_3 b_2$. The curvature and transverse shear strains can be derived as

$$\boldsymbol{\kappa} = \begin{Bmatrix} \kappa_x \\ \kappa_y \\ \kappa_{xy} \end{Bmatrix} = \begin{Bmatrix} \theta_{y,x} \\ -\theta_{x,y} \\ -\theta_{x,x} + \theta_{y,y} \end{Bmatrix} = \mathbf{B}_b \mathbf{q} = [\mathbf{B}_b^1 \ \dots \ \mathbf{B}_b^n]\mathbf{q} \tag{6}$$

$$\boldsymbol{\gamma} = \begin{Bmatrix} \gamma_{zx} \\ \gamma_{zy} \end{Bmatrix} = \begin{Bmatrix} w_{,x} + \theta_y \\ w_{,y} - \theta_x \end{Bmatrix} = \mathbf{B}_s \mathbf{q} = [\mathbf{B}_s^1 \ \dots \ \mathbf{B}_s^n]\mathbf{q} \tag{7}$$

where

$$\mathbf{q} = \{\theta_{x1} \ \ \theta_{y1} \ \ w_{o1} \ \dots \ \theta_{xn} \ \ \theta_{yn} \ \ w_{on}\}^T, \quad \mathbf{B}_b^i = \begin{bmatrix} 0 & N_{i,x} & 0 \\ -N_{i,y} & 0 & 0 \\ -N_{i,x} & N_{i,y} & 0 \end{bmatrix} \text{ and } \mathbf{B}_s^i = \begin{bmatrix} 0 & N_i & N_{i,x} \\ -N_i & 0 & N_{i,y} \end{bmatrix} \tag{8}$$

The element stiffness matrix can be computed by invoking the elemental potential energy functional which can be expressed as

$$\Pi^e = \frac{1}{2}\int_{\Omega^e} (\boldsymbol{\kappa}^T \mathbf{C}_b \boldsymbol{\kappa} + \boldsymbol{\gamma}^T \mathbf{C}_s \boldsymbol{\gamma}) d\Omega - W^e \tag{9}$$

where Ω^e denotes the planar area of the element on the x-y-plane, W^e is the work done on the element by the external load, $\mathbf{C}_b$ and $\mathbf{C}_s$ are the bending and transverse shear stiffness matrices, respectively. By substituting (7) into (9), the latter becomes

$$\Pi^e = \frac{1}{2}\mathbf{q}^T(\mathbf{K}_b^e + \mathbf{K}_s^e)\mathbf{q} - W^e = \frac{1}{2}\mathbf{q}^T \mathbf{K}^e \mathbf{q} - W^e \tag{10}$$

Where

$$\mathbf{K}^e = \mathbf{K}_b^e + \mathbf{K}_s^e, \quad \mathbf{K}_b^e = \int_{\Omega^e} \mathbf{B}_b^T \mathbf{C}_b \mathbf{B}_b d\Omega, \quad \mathbf{K}_s^e = \int_{\Omega^e} \mathbf{B}_s^T \mathbf{C}_s \mathbf{B}_s d\Omega \tag{11}$$

are the stiffness, bending stiffness and shear stiffness matrices of the element, respectively. While the displacement is continuous within the transition element, the strain/stress may be discontinuous across $\xi = 0$ and/or $\eta = 0$. It is necessary to evaluate the strain energy by partitioning the element into multiple integration zones by $\xi = 0$ and/or $\eta = 0$ as shown in Fig. 2. However, this transition element family suffers from shear locking and has little practical value in plate analyses.

2.2 The ANS elements

In the ANS method, the natural transverse shear strains at selected locations are interpolated to form the natural shear strain field. The covariant natural transverse shear strain components are (Bathe and Dvorkin 1985, Huang and Hinton 1986, Park and Stanley 1986, Sze and Zhu 1998)

$$\gamma_{z\xi} = w_{,\xi} + x_{,\xi}\theta_x - y_{,\xi}\theta_y, \quad \gamma_{z\eta} = w_{,\eta} + x_{,\eta}\theta_x - y_{,\eta}\theta_y \tag{12}$$

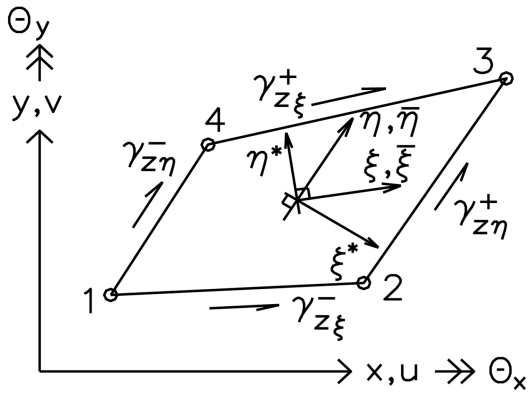

Fig. 3 Sampling of transverse shear strain and various coordinate systems for an element

A two-step interpolation scheme is employed (Donea and Lamain 1987, Choi and Park 1992, Wan 2004). In the first step, the natural strains $\gamma_{z\xi}^{-}, \gamma_{z\xi}^{+}, \gamma_{z\eta}^{-}$ and $\gamma_{z\eta}^{+}$, see Fig. 3, at the four edge mid-points are determined. Taking the edge defined by $\eta = -1$ as an example

$$\gamma_{z\xi}^{-} = \gamma_{z\xi}\Big|_{\xi=0,\,\eta=-1} \tag{13}$$

in the absence of the mid-side node. If the mid-side node or node 5 exists, the natural strain is taken to be the one interpolated at the mid-points of node 1-node 5 and node 5-node 2, i.e.

$$\gamma_{z\xi}^{-} = \frac{1-2\xi}{2}\gamma_{z\xi}\Big|_{\xi=-1/2,\,\eta=-1} + \frac{1+2\xi}{2}\gamma_{z\xi}\Big|_{\xi=+1/2,\,\eta=-1} \tag{14}$$

In the second step, $\gamma_{z\xi}^{-}$ and $\gamma_{z\xi}^{+}$ are interpolated to obtain $\gamma_{z\xi}$ whilst $\gamma_{z\eta}^{-}$ and $\gamma_{z\eta}^{+}$ are interpolated to obtain $\gamma_{z\eta}$ within the element, i.e.

$$\gamma_{z\xi} = \frac{1-\eta}{2}\gamma_{z\xi}^{-} + \frac{1+\eta}{2}\gamma_{z\xi}^{+}, \quad \text{and} \quad \gamma_{z\eta} = \frac{1-\xi}{2}\gamma_{z\eta}^{-} + \frac{1+\xi}{2}\gamma_{z\eta}^{+} \tag{15}$$

The transverse shear strain with respect to the global Cartesian coordinates can be obtained by transformation as

$$\widehat{\gamma} = \begin{Bmatrix} \gamma_{zx} \\ \gamma_{zy} \end{Bmatrix} = \mathbf{J}^{-1}\begin{Bmatrix} \gamma_{z\xi} \\ \gamma_{z\eta} \end{Bmatrix} = \widehat{\mathbf{B}}_s\mathbf{d} \tag{16}$$

in which $\mathbf{J}$ is the Jacobi matrix and $\widehat{\mathbf{B}}_s$ denotes the pertinent strain-displacement matrix. When one computes the element stiffness matrix in (11), $\mathbf{B}_s$ is replaced by $\widehat{\mathbf{B}}_s$.

The ANS scheme constructs the transverse shear strain field by sampling the strain along the element edges. In doing so, the number of independent sampled strains which constitute the numerical constraints to enforce the Kirchhoff condition can be effectively reduced in the global level and the result elements will be free from shear locking. Further discussions on ANS can be found in Dvorkin and Bathe (1984), Bathe and Dvorkin (1985), Huang and Hinton (1986), Park and Stanley (1986), Donea and Lamain (1987), Choi and Park (1992).

3. Constraints for the slave node

In early 1970's, Somervaille (1973) presented the slave-node approach in plate analysis using graded mesh. Taking the mesh in Fig. 4 as an example, the constraints to condense the transition node "*s*" are

$$(\theta_{xs}, \theta_{ys}, w_{os}) = \frac{1}{2}(\theta_{x1} + \theta_{x2}, \theta_{y1} + \theta_{y2}, w_{o1} + w_{o2}) \tag{17}$$

where nodes 1 and 2 are bounding node "*s*". The rational for the constraints is that one can formulate element ① as a four-node element as if the transition node is absent.

Fig. 5 shows an element patch which contains three transition nodes marked as "*o*". With the constraints in (17) and the four-node ANS element implemented, failures in constant moment patch tests are encountered. Furthermore, the ratios of the predicted deflections to the exact ones drop as the thickness decreases. For example, when the supporting and loading conditions corresponding to the constant moment state $M_x = 1$ and $w = w,_x = 0$ along $x = 0$ are prescribed to the mesh in Fig. 5, the ratios of the predicted deflections to exact one at the right end of the patch are 0.95, 0.24 and 0.11 for $h = 0.1$, 0.01 and 0.001. This behavior is typical for shear locking.

To explain the observation, the natural shear strains sampled along the common edge of the three elements in Fig. 4 are considered. Under the ANS scheme and the constraints in (17), the sample strains are

$$\gamma_{z\xi}^{-} = \frac{1}{2}(w_2 - w_1) + \frac{1}{4}L(\theta_1 + \theta_2) \quad \text{for element ①} \tag{18}$$

$$\gamma_{z\xi}^{+} = \frac{1}{2}(w_s - w_1) + \frac{1}{8}L(\theta_s + \theta_1) = \frac{1}{4}(w_2 - w_1) + \frac{1}{16}L(\theta_2 + 3\theta_1) \quad \text{for element ②} \tag{19}$$

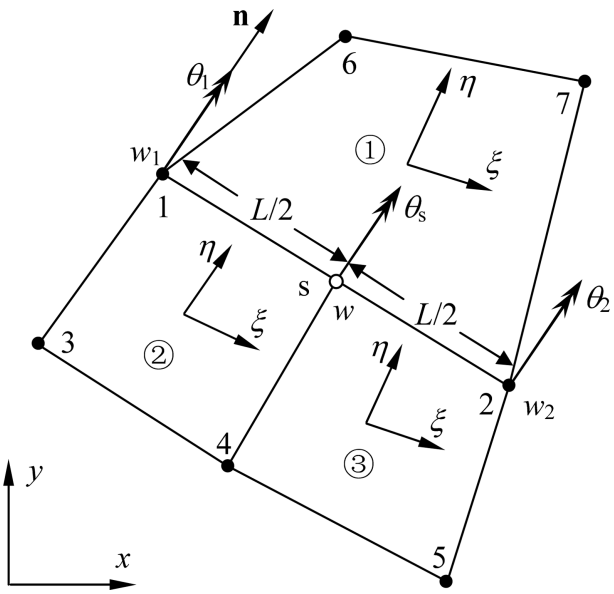

Fig. 4 A common element edge with node "*s*" being the transition node. Rotations θ_i is about vector **n** which is perpendicular to the edge

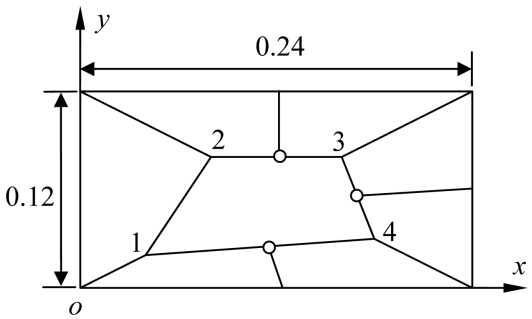

(a) Mesh for patch test

Coordinates of inner nodes

Node	x	y
1	0.04	0.02
2	0.08	0.08
3	0.16	0.08
4	0.18	0.03

E=1
v=0.25
h=0.001

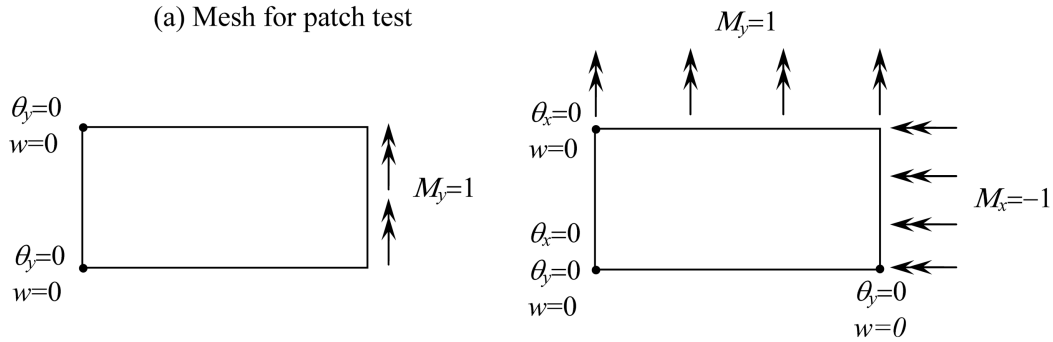

(b) Boundary conditions for constant moment M_y=1 (c) Boundary conditions for constant moment M_{xy}=1

Fig. 5 Patch test mesh and boundary conditions

$$\gamma_{z\xi}^{+} = \frac{1}{2}(w_2 - w_s) + \frac{1}{8}L(\theta_2 + \theta_s) = \frac{1}{4}(w_2 - w_1) + \frac{L}{16}(3\theta_2 + \theta_1) \text{ for element ③} \tag{20}$$

in which $\theta_i = \mathbf{n} \cdot \{\theta_{xi} \;\; \theta_{yi}\}^T$ and $\mathbf{n}$ is unit vector normal to the edge as shown in Fig. 4. As (18) equals to the sum of (19) and (20), the three strains impose two independent shear constraints which are excessive in view of the constraint index count (Hughes 1987, Saleeb and Chang 1987) for an element edge with only two active nodes.

To rectify the problem encountered by the constraints in (17), it is necessary to reduce the number of independent shear sampled along the edge. Firstly, a quadratic interpolation is employed for element ① along the common element edge, i.e.

$$\theta_i = \frac{\xi(\xi-1)}{2}\theta_1 + (1-\xi^2)\theta_s + \frac{\xi(\xi+1)}{2}\theta_2, \quad w_i = \frac{\xi(\xi-1)}{2}w_1 + (1-\xi^2)w_s + \frac{\xi(\xi+1)}{2}w_2 \tag{21}$$

where θ_i is the rotation about $\mathbf{n}$ as defined under (20). Based on the quadratic interpolation, the natural shear strain at the mid-edge, i.e., node "s", is

$$\gamma_{z\xi}^{-} = \frac{1}{2}(w_2 - w_1) + \theta_s \text{ for element ①} \tag{22}$$

To reduce the number of independent shear sampled along the edge to one, θ_s and w_s are solved by equating the strains sampled by the three elements along their common edge. In other words

$$\gamma_{z\xi}^{-} \text{ of element ①} = \gamma_{z\xi}^{+} \text{ of element ②} = \gamma_{z\xi}^{+} \text{ of element ③} \tag{23}$$

and the involved terms have been given in (19), (20) and (22). From the requirement

$$\theta_s = \frac{\theta_1 + \theta_2}{2}, \quad w_s = \frac{w_1 + w_2}{2} + \frac{L}{8}(\theta_2 - \theta_1) \tag{24}$$

As θ_i is obtained from θ_x and θ_y by projection, the above constraints can readily be satisfied by

$$\begin{Bmatrix} \theta_{xs} \\ \theta_{ys} \end{Bmatrix} = \frac{1}{2}\left(\begin{Bmatrix} \theta_{x1} \\ \theta_{y1} \end{Bmatrix} + \begin{Bmatrix} \theta_{x2} \\ \theta_{y2} \end{Bmatrix} \right), \quad w_s = \frac{w_1 + w_2}{2} + \frac{L}{8}\mathbf{n} \cdot \left(\begin{Bmatrix} \theta_{x2} \\ \theta_{y2} \end{Bmatrix} - \begin{Bmatrix} \theta_{x1} \\ \theta_{y1} \end{Bmatrix} \right) \tag{25}$$

With the above constraints, (22) reduces to (18). In other words, the element containing transition nodes as their mid-side nodes can be continued to be formulated as an four-node ANS element.

Comparing the constraints in (17) and (25), the present constraint on w_s depends on not only the deflections but also the rotations of the nodes 1 and 2. Obviously, it leads to displacement incompatibility which, however, is often regarded only as a sufficient but not necessary requirement for convergence. A relaxed and practical requirement is the patch test fulfillment which indeed has been used in developing many successful incompatible displacement and enhanced strain elements (Taylor *et al.* 1976, Simo and Rifai 1990, Sze and Chow 1991a). With the constraints in (25) implemented, constant moment patch tests conducted by using the mesh in Fig. 5 are exercised and passed. Hence, the incompatibility is acceptable and convergence is secured.

An interesting point on the new constraints on the slave node is that they turn out to be identical to the discrete Kirchhoff constraints employed to define the DOFs of the mid-side slave nodes in the well-known discrete Kirchhoff elements (Batoz 1982, Batoz and Tahar 1982).

4. Hybrid stress C^0 plate bending element

The old and new constraints for the slave node as well as the ANS transition element family decribed in Section 2 are implemented for *h*-adaptive analyses. The four-node ANS element is employed in all implementations. For completeness, the key *h*-adaptive procedures on the error estimation and the stress recovery are briefly described in Appendices A and B. On the basis of the number of DOFs, the slave-node approach using the new constraints is often markedly more accurate than the transition-element approach which, in turn, is often markedly more accurate than the slave-node approach using the old constraints. Examples will be presented in the next section for illustration.

Following the success of the new constraints in the slave-node approach which uses only the four-node element, this section aims to present a hybrid ANS element which can yield better accuracy than the four-node ANS elements.

4.1 Element stiffness matrix of the hybrid ANS element

The elemental Hellinger-Reissner functional that employs an ANS shear strain field can be written as (Lee and Pain 1978)

$$\Pi_{HR}^{e} = \int_{\Omega^e} \left[-\frac{1}{2}\mathbf{M}^T\mathbf{C}_b^{-1}\mathbf{M} - \frac{1}{2}\mathbf{Q}^T\mathbf{C}_s^{-1}\mathbf{Q} + \mathbf{M}^T\boldsymbol{\kappa} + \mathbf{Q}^T\widehat{\boldsymbol{\gamma}} \right] d\Omega - W^e \tag{26}$$

where $\mathbf{M} = \{M_x, M_y, M_z\}^T$ and $\mathbf{Q} = \{Q_{zx}, Q_{zy}\}^T$ are respectively the vectors of independently assumed moments and shear forces. The ANS transverse shear strain $\widehat{\gamma}$ is employed to avoid shear locking. $\mathbf{M}$ and $\mathbf{Q}$ can be expressed as

$$\mathbf{M} = \mathbf{P}_b\boldsymbol{\beta}, \quad \mathbf{Q} = \mathbf{P}_s\boldsymbol{\beta} \tag{27}$$

in which $\mathbf{P}_b$ and $\mathbf{P}_s$ are the shape function matrixes and $\boldsymbol{\beta}$ is the vector of coefficients. Substitution of (6), (16), (27) into (26) gives

$$\Pi_{HR}^e = -\frac{1}{2}\boldsymbol{\beta}^T\mathbf{H}\boldsymbol{\beta} + \boldsymbol{\beta}^T\mathbf{G}\boldsymbol{\beta} - W^e \tag{28}$$

where

$$\mathbf{H} = \int_{\Omega^e}(\mathbf{P}_b^T\mathbf{C}_b^{-1}\mathbf{P}_b + \mathbf{P}_s^T\mathbf{C}_s^{-1}\mathbf{P}_s)d\Omega, \quad \mathbf{G} = \int_{\Omega^e}(\mathbf{P}_b^T\mathbf{B}_b + \mathbf{P}_s^T\widehat{\mathbf{B}}_b)d\Omega \tag{29}$$

As each element possesses its own set of the assumed moments and shear forces, the stationary nature of the functional with respect to $\boldsymbol{\beta}$ leads to

$$\mathbf{H}\boldsymbol{\beta} = \mathbf{G}\mathbf{q} \tag{30}$$

Back substitution of (30) into (28) results in

$$\Pi_{HR}^e = \frac{1}{2}\mathbf{q}^T(\mathbf{G}^T\mathbf{H}^{-1}\mathbf{G})\mathbf{q} - W^e \tag{31}$$

in which the embraced term is the element stiffness matrix.

4.2 Hybrid stress element family with twelve moment and shear force modes

Before devising the moment and shear force modes, the three hybrid C^0 plate elements in Saleeb and Chang (1987), Weissman and Taylor (1990), Ayad *et al.* (1998) are tested by some popular benchmark problems. It is noted that the element with equilibrating moment and shear force fields by Ayad *et al.* (1998) is most accurate. The element employs the following assumed moments

$$\mathbf{M} = \begin{Bmatrix} M_x \\ M_y \\ M_{xy} \end{Bmatrix} = \begin{bmatrix} 1 & 0 & 0 & \xi & \eta & \xi\eta & 0 & 0 & 0 & 0 & 0 & 0 \\ 0 & 1 & 0 & 0 & 0 & 0 & \xi & \eta & \xi\eta & 0 & 0 & 0 \\ 0 & 0 & 1 & 0 & 0 & 0 & 0 & 0 & 0 & \xi & \eta & \xi\eta \end{bmatrix} \begin{Bmatrix} \beta_1 \\ \vdots \\ \beta_{12} \end{Bmatrix} \tag{32}$$

which are bilinear in (ξ, η). The assumed shear modes are derived from the equilibrium conditions, i.e.

$$Q_{zx} = M_{x,x} + M_{xy,y}, \quad Q_{zy} = M_{xy,x} + M_{y,y} \tag{33}$$

The conditions lead to rather length expressions on the shear force modes as

$$\frac{\partial}{\partial x} = \frac{b_3 + b_2\xi}{J}\frac{\partial}{\partial \xi} - \frac{b_1 + b_2\eta}{J}\frac{\partial}{\partial \eta}, \quad \frac{\partial}{\partial y} = -\frac{a_3 + a_2\xi}{J}\frac{\partial}{\partial \xi} + \frac{b_3 + b_2\xi}{J}\frac{\partial}{\partial \eta}$$

where J have been defined in (5).

However, the shear modes can be simplified by employing skew coordinates to define the moment modes. In this light, the skew coordinates (ξ^*, η^*) of Sze and Chow (1991b) can be employed

$$\xi^* = a_1(x-x_0)+b_1(y-y_0) = (a_1^2+b_1^2)\xi+(a_1a_3+b_1b_3)\eta+(a_1a_2+b_1b_2)\xi\eta$$
$$\eta^* = a_3(x-x_0)+b_3(y-y_0) = (a_3^2+b_3^2)\eta+(a_3a_1+b_3b_1)\xi+(a_2a_3+b_2b_3)\xi\eta$$

The other alternatives $(\bar{\xi},\bar{\eta})$ given by Yuan *et al.* (1993)

$$\bar{\xi} = \xi-\frac{J_2}{J_0}\xi\eta = \frac{1}{J_0}(b_3(x-x_0)-a_3(y-y_0)), \quad \bar{\eta} = \eta-\frac{J_1}{J_0}\xi\eta = \frac{1}{J_0}(-b_1(x-x_0)+a_1(y-y_0))$$

can also be employed. It is trivial to show that

$$\xi^*\perp\eta, \quad \eta^*\perp\xi, \quad \frac{\partial\xi^*}{\partial x}=a_1, \ \frac{\partial\eta^*}{\partial x}=a_3, \ \frac{\partial\xi^*}{\partial y}=b_1, \ \frac{\partial\eta^*}{\partial y}=b_1$$
$$\bar{\xi}\parallel\xi, \quad \bar{\eta}\parallel\eta, \quad \frac{\partial\bar{\xi}}{\partial x}=\frac{b_3}{J_o}, \ \frac{\partial\bar{\eta}}{\partial x}=-\frac{b_1}{J_o}, \ \frac{\partial\bar{\xi}}{\partial y}=-\frac{a_3}{J_o}, \ \frac{\partial\bar{\eta}}{\partial y}=\frac{a_1}{J_o}$$

Using the two coordinate systems, two elements can be derived. With (ξ, η) replaced by (ξ^*, η^*) in (32), the related assumed shear force as derived from (33) would be

$$\mathbf{Q} = \begin{bmatrix} \mathbf{0}_{2\times3} & \begin{matrix} a_1 & a_3 & a_1\eta^*+a_3\xi^* \\ 0 & 0 & 0 \end{matrix} & \begin{matrix} 0 & 0 & 0 \\ b_1 & b_3 & b_1\eta^*+b_3\xi^* \end{matrix} & \begin{matrix} b_1 & b_3 & b_1\eta^*+b_3\xi^* \\ a_1 & a_3 & b_1\eta^*+a_3\xi^* \end{matrix} \end{bmatrix} \begin{Bmatrix} \beta_1 \\ \vdots \\ \beta_{12} \end{Bmatrix} \tag{34}$$

and the related element will be designated as HSP1. With (ξ, η) replaced by $(\bar{\xi},\bar{\eta})$ in (32), the related assumed shear force as derived from (33) would be

$$\mathbf{Q} = \frac{1}{J_0}\begin{bmatrix} \mathbf{0}_{2\times3} & \begin{matrix} b_3 & -b_1 & b_3\bar{\eta}-b_1\bar{\xi} \\ 0 & 0 & 0 \end{matrix} & \begin{matrix} 0 & 0 & 0 \\ -a_3 & a_1 & -a_3\bar{\eta}+a_1\bar{\xi} \end{matrix} & \begin{matrix} -a_3 & a_1 & -a_3\bar{\eta}+a_1\bar{\xi} \\ b_3 & -b_1 & b_3\bar{\eta}-b_1\bar{\xi} \end{matrix} \end{bmatrix} \begin{Bmatrix} \beta_1 \\ \vdots \\ \beta_{12} \end{Bmatrix} \tag{35}$$

and the related element will be designated as HSP2. It is obvious that both elements are identical when the elements are rectangular in shape.

5. Numerical examples

In this section, several popular benchmark tests will be studied by the few presented adaptive strategies on the elements and/or slave-node constraints. The following abbreviations will be employed in presenting the results:

- ANS-T: the transition element family reviewed in Section 2. The four-node element is also formulated by ANS.

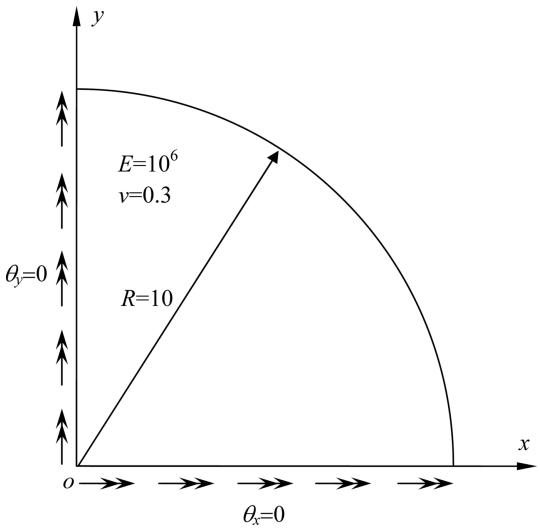

Fig. 6 One quarter of a circular plate

- ANS-C*: the slave-node approach that adopts the conventional constraints in and the four-node ANS element is employed.
- ANS-C: the slave-node approach that adopts the newly developed constraints in and the four-node ANS element is employed.
- HSP1-C, HSP2-C: the slave-node approaches that adopt the newly developed constraints in whilst the new four-node hybrid elements HSP1 and HSP2 (see Section 4.2) are employed, respectively.
- HSP-C: in the cases that HSP1-C and HSP2-C produce graphically indistinguishable results, the results will be jointly presented as HSP-C for clarity.

To complete the adaptive analysis, the super convergent patch recovery technique proposed by Zienkiewicz and Zhu (1992a, b) is applied to produce smoothed stress field with improved accuracy. Meanwhile, the error estimator proposed by Zienkiewicz and Zhu (1987) is employed to estimate the system and element errors.

The log-log plots for $\|\mathbf{e}\|$ (error in energy norm) versus nDOF (the number of active DOFs) will be presented. Besides the thin circular plate examples in which analytical solutions are known, errors for all other examples are obtained by estimation as briefed in the two appendices.

In the conventional refinement strategy, the criterion for subdividing an element is based on a fixed percentage of the estimated error. When this refinement strategy is employed, the portion of the elements that contain transition nodes as their mid-side nodes is small and typically between 5% and 10%. For the sake of studying the performance of different adaptive strategies, the optimal refinement strategy of Lee and Lo (1999) is adopted to increase this ratio. Instead of using a fixed target relative error in each adaptive refinement step, Lee and Lo (1999) employ the following target relative error

$$\eta_i = \eta_{i-1} - (\eta_0 - \eta_t)\frac{r^{n-i}(r-1)}{r^n - 1} \quad (1 \le i \le n) \tag{36}$$

in which η_i is the target relative error for the current step, $\eta_{i\text{-}1}$ is the estimated relative error of the

previous step, η_0 is the estimated relative error in the first step, η_t is the prescribed final target relative error, n is the prescribed maximum number of adaptive steps and r is a key parameter to decide the convergence speed. In order to raise the afore-mentioned element portion, r is set to 1.5 whilst r equals unity for the conventional strategy.

In the following examples, only the adaptively generated meshes based on HSP2-C are shown for keeping the paper in reasonable long.

5.1 Patch tests

The employed mesh is shown in Fig. 5 which contains three transition nodes and is similar to that of MacNeal and Harder (1985). The supporting and loading conditions corresponding to several different constant moment states are prescribed. Among ANS-T, ANS-C*, ANS-C, HSP1-C and HSP2-C, only ANS-C* which adopts the conventional slave-node constraints fails the patch tests.

5.2 Clamped circular plate subjected to central point load

A circular plate of radius $R = 10$ subjected to a central point load is considered. Owing to symmetry, one quarter of the plate is modeled as shown in Fig. 6. Along the x- and y-axes, the conditions of symmetry are applied. The circumference is fully-clamped. To test the adaptive strategies for thick and thin plates, R/h = 5, 50 and 500 are considered. For all R/h ratios, the target relative error is set to be 3%. Figs. 7, 8 and 9 show the meshes for R/h = 5, 50 and 500, respectively. Owing to the stress singularity under the central point load, the element density around the central is highest. Errors of different adaptive strategies are compared in Figs. 10, 11 and 12 for R/h = 5, 50, and 500, respectively. For R/h = 5, ANS-T and HSP-C require the highest and lowest nDOF to attain the target relative error, respectively. As the plate is extremely thick, ANS-C and ANS-C* yield virtually identical results. The pitfall of ANS-C* becomes obvious when the plate get thinner as seen in Figs. 11 and 12 in which ANS-C* becomes the worst performer followed by

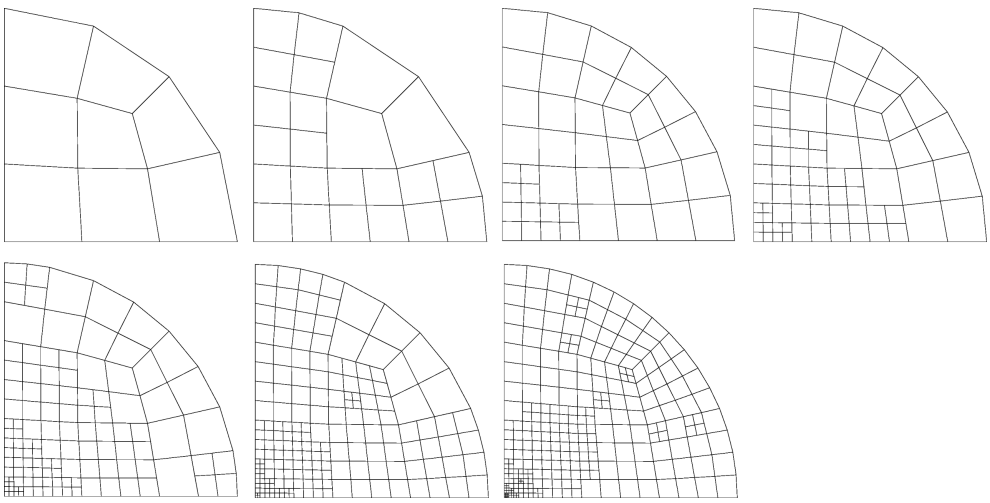

Fig. 7 Adaptive meshes for the clamped circular plate with R/h = 5 subjected to central point load

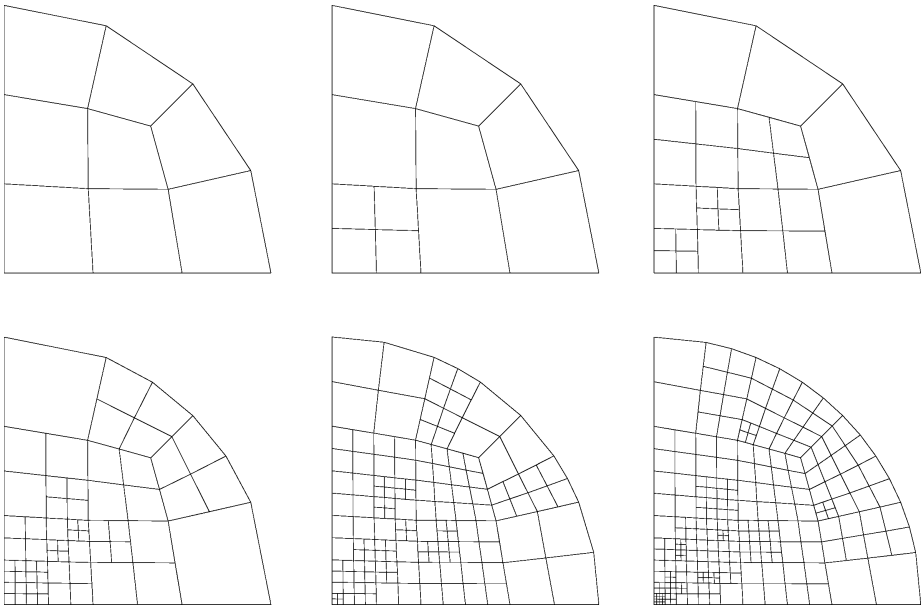

Fig. 8 Adaptive meshes for the clamped circular plate with $R/h = 50$ subjected to central point load

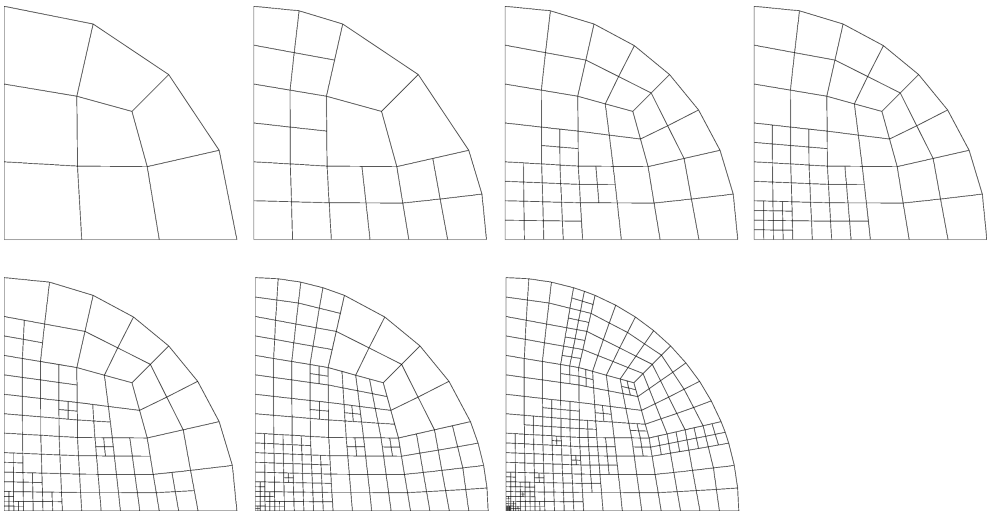

Fig. 9 Adaptive meshes for the clamped circular plate with $R/h = 500$ subjected to central point load

ANS-T and the ANS-C. The best performer remains to be HSP-C which uses not only the least nDOF but also the least number of steps to attain the target relative error.

The predictions of ANS-C* are rather consistent. For very thick plate, it yields nearly identical results as ANS-C. As the plate becomes moderately thick, the errors of ANS-C* starts to exceed those of ANS-T. In light of this consistent behavior, the predictions of ANS-C* will be dropped in the subsequent comparisons for conciseness.

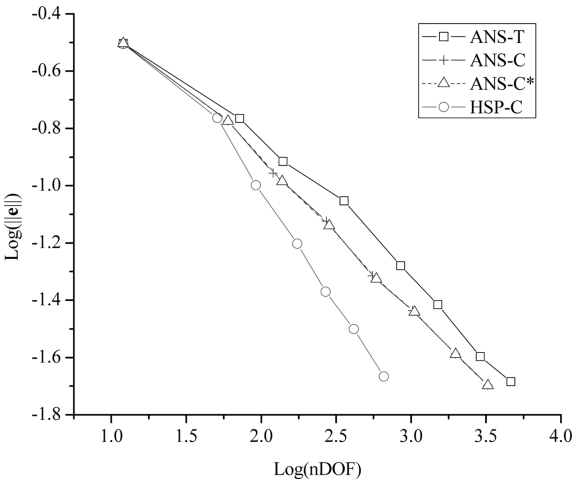

Fig. 10 Errors of different adaptive strategies for the clamped circular plate with $R/h = 5$ subjected to central point load

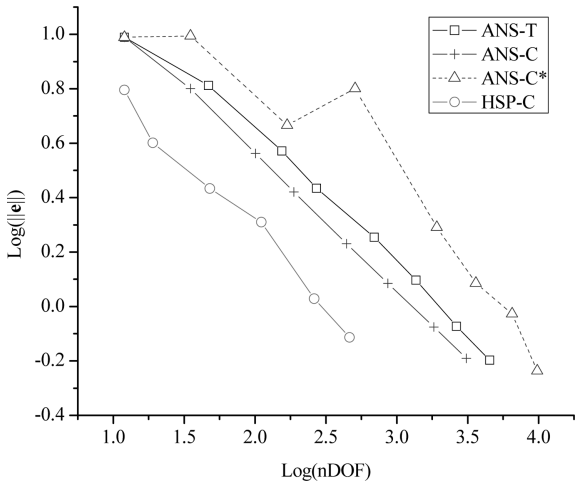

Fig. 11 Errors of different adaptive strategies for the clamped circular plate with $R/h = 50$ subjected to central point load

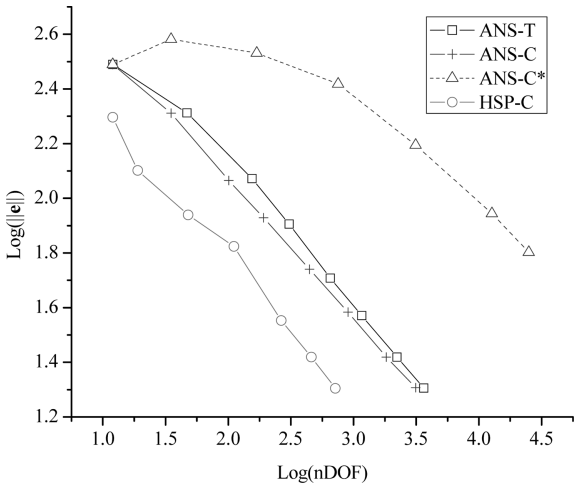

Fig. 12 Errors of different adaptive strategies for the clamped circular plate with R/h = 500 subjected to point load

5.3 Simply-supported circular plate subjected to central point load

This example considers the same circular plates as in the last example except that the circumference is now simply-supported. For both R/h = 5 and 500, the target relative error is set to be 3%. The pertinent adaptive meshes are portrayed in Figs. 13 and 14. Again, the element density around the central is highest due to the central point load. Comparisons between different adaptive strategies are presented in Figs. 15 and 16. It can be seen that HSP-C uses one step fewer than ANS-T and ANS-C to achieve the target relative error for both R/h ratios.

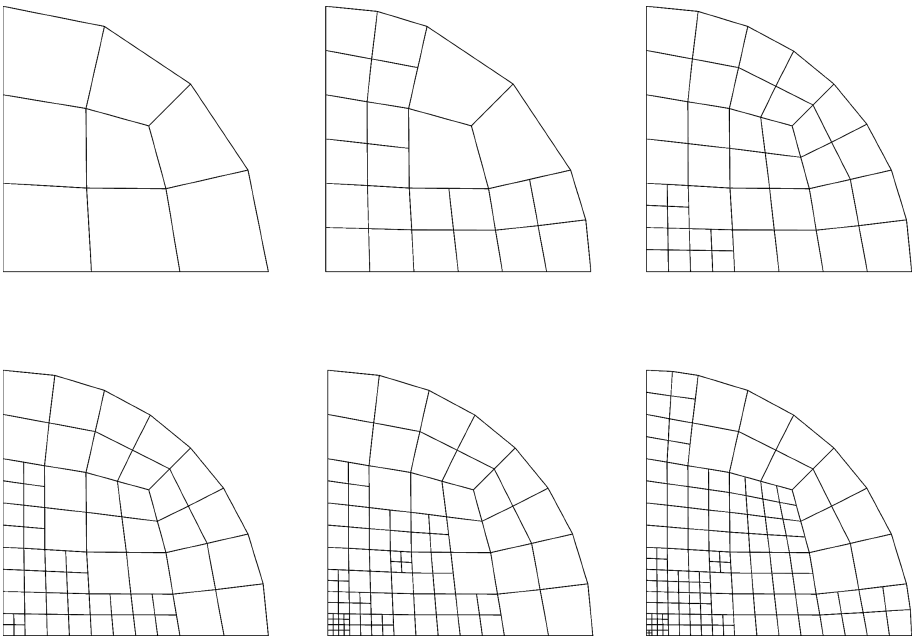

Fig. 13 Adaptive meshes for the simply-supported circular plate with R/h = 5 subjected to central point load

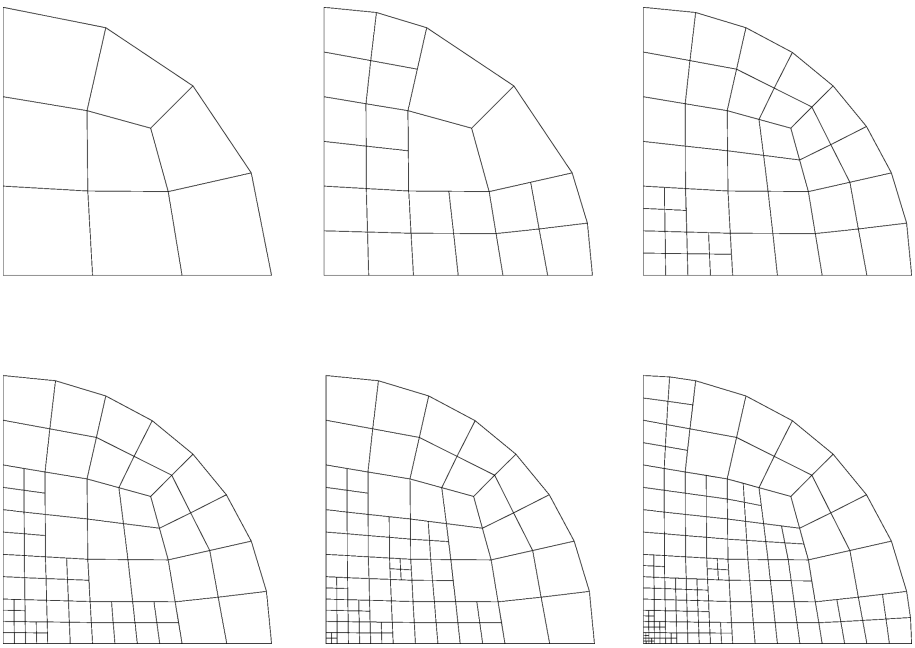

Fig. 14 Adaptive meshes for the simply-supported circular plate with R/h = 500 subjected to central point load

5.4 Clamped rhombic plate subjected to central point load

A rhombic plate with side length L and thickness h is considered. All edges of the plate are fully-

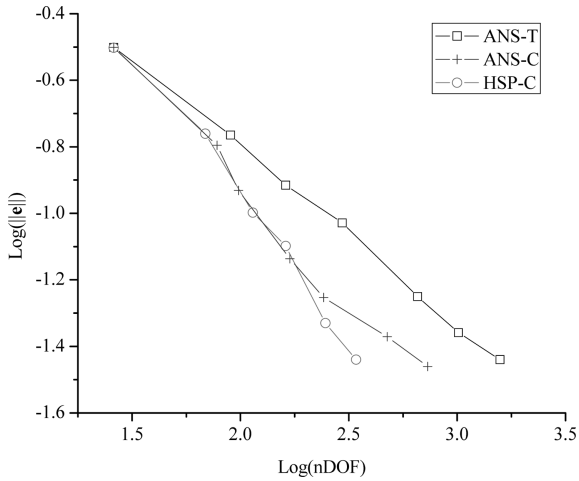

Fig. 15 Errors of different adaptive strategies for the simply-supported circular plate with R/h = 5 subjected to central point load

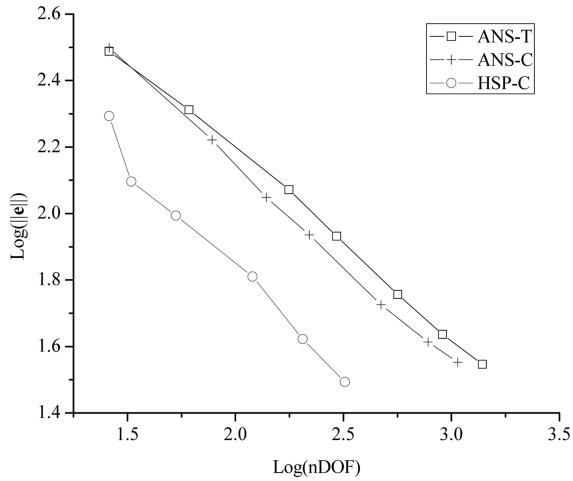

Fig. 16 Errors of different adaptive strategies for the simply supported circular plate with R/h = 500 subjected to central point load

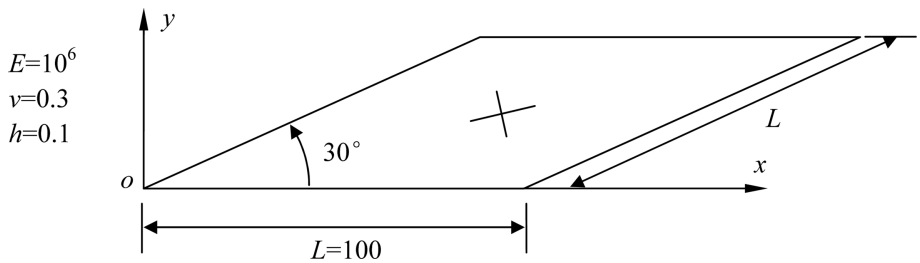

Fig. 17 The rhombic plate problem

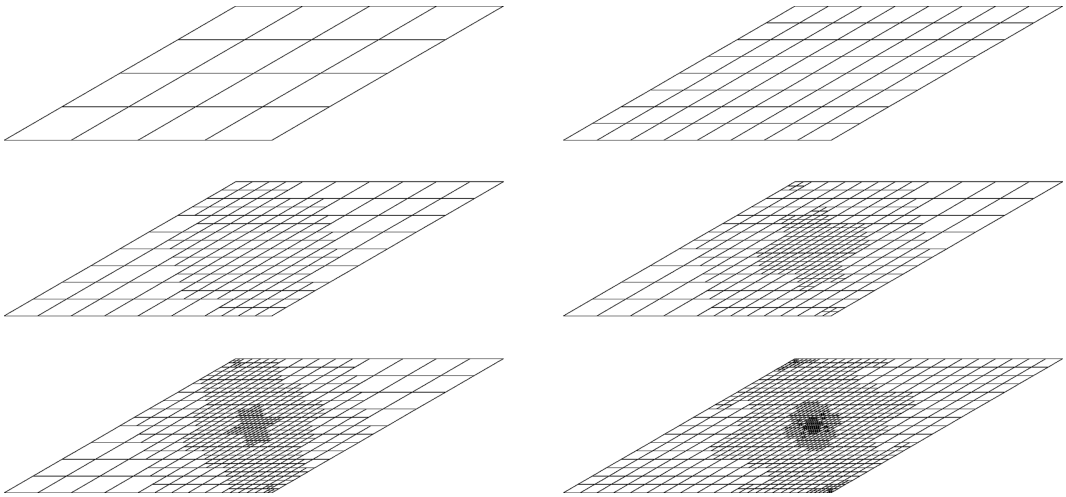

Fig. 18 Adaptive meshes for the clamped rhombic plate with L/h = 1000 subjected to central point load

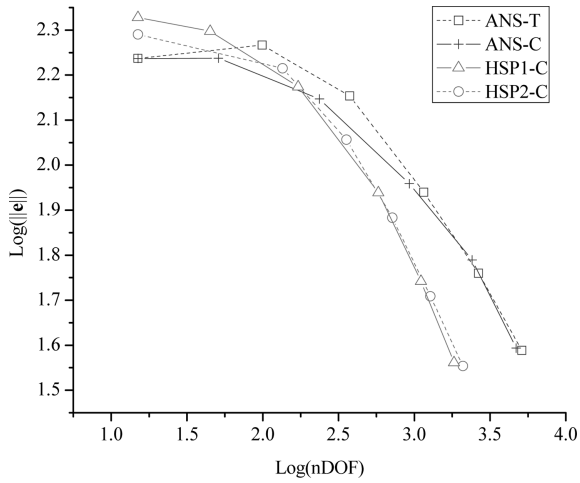

Fig. 19 Errors of different adaptive strategies for the clamped rhombic plate with L/h = 1000 subjected to central point load

clamped and a point force is applied to the centre of the plate. The whole plate is modeled and analyzed as shown in Fig. 17. The plate aspect ratio $L/h = 1000$ is considered. The target relative error is set to be 10%. The corresponding adaptive meshes can be seen in Fig. 18. Owing to the stress singularity induced by the point load, the element density is highest at the plate centre. Errors of different elements and adaptive strategies are compared in Fig. 19. Unlike the previous examples, HSP1-C and HSP2-C produce slightly different results.

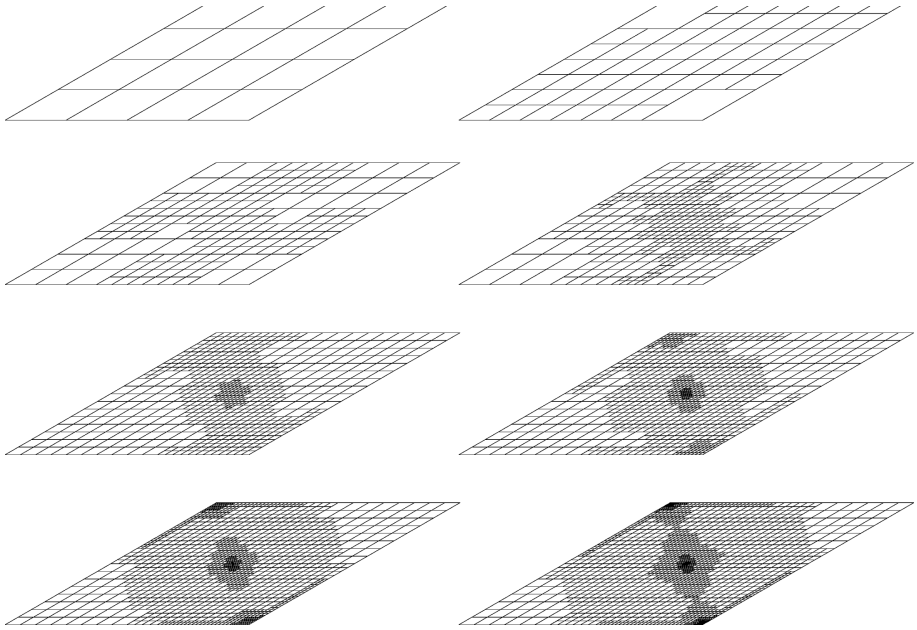

Fig. 20 Adaptive meshes for the simply-supported rhombic plate with L/h = 1000 subjected to central point load

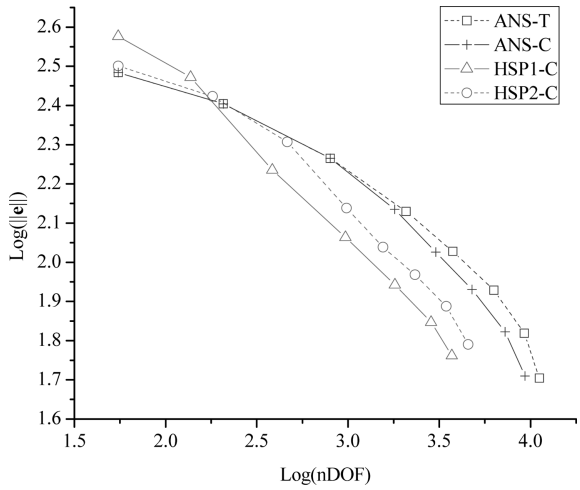

Fig. 21 Errors of different adaptive strategies for the simply-supported rhombic plate with L/h = 1000 subjected to point load problem

5.5 Simply-supported rhombus plate subjected to central point load

In this example, the last rhombic plate under the same loading is considered again. However, its edges are now simply-supported. The target relative error is set to be 10%. The pertinent adaptive meshes are portrayed in Fig. 20. Unlike the last examples, stress singularities exist not only under the point load but also at the obtuse corners. Hence, high element densities can be noted at these locations. Errors of different elements and adaptive strategies are compared in Fig. 21. In this example, the difference between HSP1-C and HSP2-C becomes obvious. HSP1-C uses not only fewer nDOF but also one fewer step than HSP2-C in attaining the target relative error.

5.6 Simply-supported rhombus plate subjected to uniform load

All the previous circular and rhombic plate examples consider point load. In the present example, the previous rhombic plate is loaded by uniform pressure. The target relative error is again set to be 10%. The pertinent adaptive meshes are presented in Fig. 22. Unlike the last two examples, stress singularities exist only at the two obtuse corners. Hence, the element density at the centre is relative low. Errors of different adaptive strategies are compared in Fig. 23. Similar as the last example, HSP1-C uses fewer nDOF and one fewer step than HSP2-C to achieve the target relative error.

5.8 Discussions on results

In the above examples, the error estimation scheme manages to detect the stress concentrations and the adaptive refinement scheme refines the elements at and around the stress concentrations. The refinement strategies comprising various elements and, if applicable, slave-node constraints are tested for plates with different thicknesses. For very thick plates, ANS-C* and ANS-C yield nearly identical results which are more accurate than those of ANS-T. For moderately thick plates, the errors of ANS-C* starts to exceed those of ANS-T whilst ANS-C remains to be more accurate than

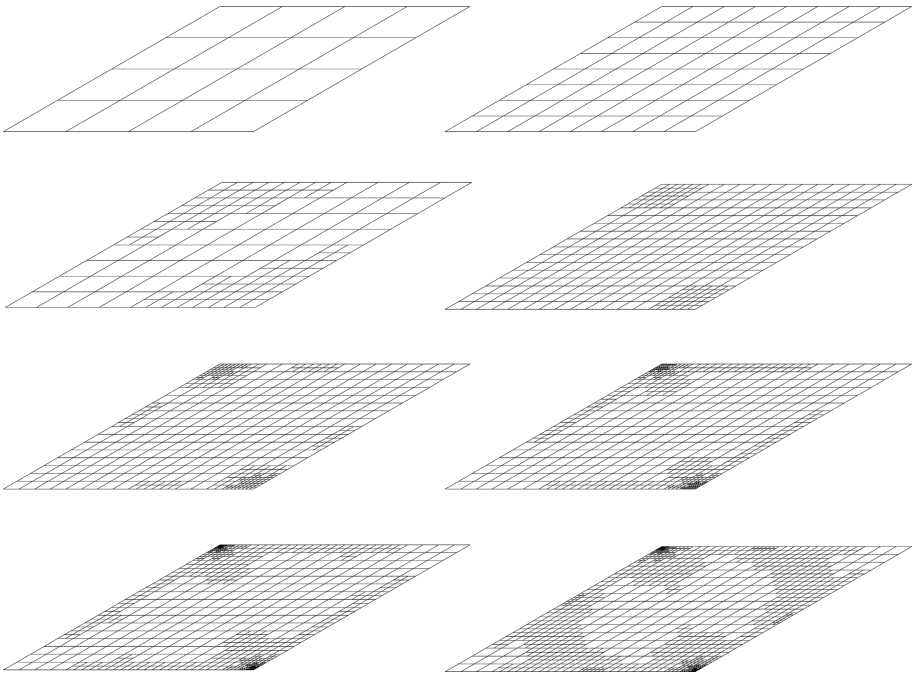

Fig. 22 Adaptive meshes for the simply-supported rhombic plate with L/h = 1000 subjected to uniform load

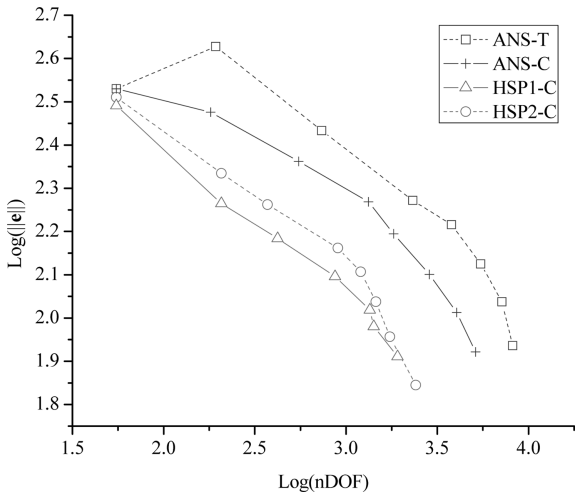

Fig. 23 Errors of different adaptive strategies for the simply-supported rhombic plate with L/h = 1000 subjected to uniform load

ANS-T. Generally speaking, to attain the same target accuracy, HSP1-C requires the least nDOF followed by HSP2-C, ANS-C, ANS-T and, finally, ANS-C*. Sometimes, ANS-C has to attain the same target accuracy by one more refinement step than HSP1-C and HSP2-C. The most distinctive example is the quarter circular plate with a reentrant corner. HSP1-C and HSP2-C use only 2085 DOFs to reduce error norm below 3% whilst ANS-T has to use 5535 DOFs.

6. Conclusions

The following concluding remarks can be drawn after studying the various elements and slave-node constraints by the benchmark problems:

1. The conventional slave-node constraints of Somervaille (1973) leads to constant moment patch test failure. In thin and moderately thick plates, the constraints also lead to poor finite element predictions.
2. The new slave-node constraints which turns out to the same as the discrete Kirchhoff constraints (Batoz 1982, Batoz and Tahar 1982) resolve the constant moment patch test failure. It also sharply improves the accuracy of the slave-node approach in thin and moderately thick plate problems.
3. When co-used with the four-node ANS element, the new slave-node constraints yield markedly more accurate results than the ANS transition element family in which the transition nodes are active.
4. The formulation of the four-node ANS hybrid elements of Ayad *et al.* (1998) is simplified by respectively employing the skew coordinates by respectively Sze and Chow (1991b) and Yuan *et al.* (1993) to define the assumed moment and shear force modes,. Similar to the studies conducted by Sze (1994b) on hybrid C^1 and semi-Loof plate elements, the element employing the coordinates of Sze and Chow is more accurate than the one employing the coordinates of Yuan *et al.* (1993). However, the difference becomes appreciable only when the mesh distortion is considerably large.
5. When co-used with the new slave-node constraints, the two proposed four-node ANS hybrid elements yield markedly more accurate results than the four-node ANS element. In a number of examples, the ANS element has to attain the same target accuracy by one more refinement step than the two hybrid ANS elements.
6. Though there is computation cost for condensing the transition nodes in the slave-node approach, the condensation can be done in the element level. The reduction in nodal DOFs with respect to the transition element family for the same accuracy appears to be sufficiently large to offset the condensation cost, not to mention that the transition element family also requires some computation treatments which are not needed in the slave-node approach.

References

Ayad, R., Dhatt, G. and Batoz, J.L. (1998), "A new hybrid-mixed variational approach for Reissner-Mindlin plates. The MiSP model", *Int. J. Numer. Meth. Eng.*, **42**(7), 1149-1179.

Bathe, K.J. and Dvorkin, E.N. (1985), "A four-node plate bending element based on Mindlin/Reissner plate theory and a mixed interpolation", *Int. J. Numer. Meth. Eng.*, **21**(2), 367-383.

Batoz, J.L. (1982), "Explicit formulation for an efficient triangular plate-bending element", *Int. J. Numer. Meth. Eng.*, **18**(7), 1077-1089.

Batoz, J.L. and Tahar, M.B. (1982), "Evaluation of a new quadrilateral thin plate bending element", *Int. J. Numer. Meth. Eng.*, **18**(11), 1655-1677.

Choi, C.K. and Lee, E.J. (2004), "Nonconforming variable-node axisymmetric solid element", *J. Eng. Mech.*, **130**(5), 578-588.

Choi, C.K. and Park, Y.M. (1992), "Transition plate-bending elements for compatible mesh gradation", *J. Eng. Mech.*, **118**(3), 462-480.

Choi, C.K. and Park, Y.M. (1997), "Conforming and nonconforming transition plate bending elements for an adaptive h-refinement", *Thin Wall. Struct.*, **28**(1), 1-20.

Devloo, P., Oden, J.T. and Strouboulis, T. (1987), "Implementation of an adaptive refinement technique for the SUPG algorithm", *Comput. Meth. Appl. Mech. Eng.,* **61**(3), 339-358.

Donea, J. and Lamain, L.G. (1987), "A modified representation of transverse shear in C^0 quadrilateral plate elements", *Comput. Meth. Appl. Mech. Eng.* **63**(2), 183-207.

Dvorkin, E.N. and Bathe, K.J. (1984), "A continuum mechanics based four-node shell element for general nonlinear analysis", *Eng. Comput. (Swansea, Wales)*, **1**(1), 77-88.

Gupta, A.K. (1978), "A finite element for transition from a fine to a coarse grid", *Int. J. Numer. Meth. Eng.*, **12**(1), 35-45.

Huang, H.C. and Hinton, E. (1986), "A new nine node degenerated shell element with enhanced membrane and shear interpolation", *Int. J. Numer. Meth. Eng.*, **22**(1), 73-92.

Hughes, J.R. (1987), "The finite element method : linear static and dynamic finite element analysis", Englewood Cliffs, Prentice-Hall.

Lee, C.K. and Lo, S.H. (1999), "A full 3D finite element analysis using adaptive refinement and PCG solver with back interpolation", *Comput. Meth. Appl. Mech. Eng.*, **170**, 39-64.

Lee, S.W. and Pain, T.H.H. (1978), "Improvement of plate and shell finite elements by mixed formulations", *AIAA J.*, **16**(1), 29-34.

Lee, S.W., Wong, S.C. and Rhiu, J.J. (1985), "Study of the nine-node mixed formulation finite element for thin plates and shells", *Comput. Struct.*, **21**(6), 1325-1334.

Lo, S.H., Wan, K.H. and Sze, K.Y. (2006), "Adaptive refinement analysis using hybrid-stress transition elements", *Comput. Struct.*, **84**, 2212-2230.

MacNeal, R.H. and Harder, R.L. (1985), "A proposed standard set of problems to test finite element accuracy", *Finite Elem. Analy. Des.*, **1**(1), 3-20.

Park, K.C. and Stanley, G.M. (1986), "A curved C^0 shell element based on assumed natural coordinate strains", *J. Appl. Mech-T. ASME*, **53**(2), 278-290.

Saleeb, A.F. and Chang, T.Y. (1987), "An efficient quadrilateral element for plate bending analysis", *Int. J. Numer. Meth. Eng.*, **24**(6), 1123-1155.

Simo, J.C. and Rifai, M.S. (1990), "Class of mixed assumed strain methods and the method of incompatible modes", *Int. J. Numer. Meth. Eng.*, **29**(8), 1595-1638.

Somervaille, I.J. (1973), "A technique for mesh grading applied to conforming plate bending finite elements", *Int. J. Numer. Meth. Eng.*, **6**(2), 310-312.

Sze, K.Y. (1994a), "An explicit hybrid-stabilized 9-node Lagrangian shell element", *Comput. Meth. Appl. Mech. Eng.,* **117**(3-4), 361-379.

Sze, K.Y. (1994b), "Minimal assumed moments and optimal local coordinates for plate elements based upon the complementary energy functional", *Comput. Mech.*, **14**(6), 586-595.

Sze, K.Y. and Chow, C.L. (1991a), "Incompatible element for axisymmetric structure and its modification by hybrid method", *Int. J. Numer. Meth. Eng.*, **31**(2), 385-405.

Sze, K.Y. and Chow, C.L. (1991b), "Efficient hybrid quadrilateral Kirchhoff plate bending element", *Int. J. Numer. Meth. Eng.*, **32**(1), 149-169.

Sze, K.Y. and Zhu, D. (1998), "Quadratic assumed natural strain triangular element for plate bending analysis", *Commun. Numer. Meth. Eng.*, **14**(11), 1013-1025.

Taylor, R.L., Beresford, P.J. and Wilson, E.L. (1976), "A non-conforming element for stress analysis", *Int. J. Numer. Meth. Eng.*, **10**(6), 1211-1219.

Wan, K.H. (2004), "Transition finite elements for mesh refinement in plane and plate bending analysis", M.Ph. Thesis, Department of Mechanical Engineering, The University of Hong Kong.

Weissman, S.L. and Taylor, R.L. (1990), "Resultant fields for mixed plate bending elements", *Comput. Meth. Appl. Mech. Eng.,* **79**(3), 321-355.

Yuan, K.Y., Huang, Y.S. and Pian, T.H.H. (1993), "New strategy for assumed stresses for 4-node hybrid stress membrane element", *Int. J. Numer. Meth. Eng.*, **36**(10), 1747-1763.

Zienkiewicz, O.C. and Zhu, J.Z. (1987), "A simple error estimator and adaptive procedure for practical engineering analysis", *Int. J. Numer. Meth. Eng.*, **24**(2), 337-357.

Zienkiewicz, O.C. and Zhu, J.Z. (1992a), "Superconvergent patch recovery and a posteriori error estimates. Part 1: the recovery technique", *Int. J. Numer. Meth. Eng.*, **33**(7), 1331-1364.

Zienkiewicz, O.C. and Zhu, J.Z. (1992b), "Superconvergent patch recovery and a posteriori error estimates. Part 2: error estimates and adaptivity", *Int. J. Numer. Meth. Eng.*, **33**(7), 1365-1382.